Received: 18 August 2017 | Revised: 7 January 2018 | Accepted: 8 January 2018

DOI: 10.1002/mrm.27112

FULL PAPER

Magnetic Resonance in Medicine

# Diffusion MRI Monitoring of Specific Structures in the Irradiated Rat Brain

**Julie Constanzo[1] | Matthieu Dumont[3] | Réjean Lebel[4] | Luc Tremblay[4] | Kevin Whittingstall[4] | Laurence Masson-Côté[1,2] | Sameh Geha[6] | Philippe Sarret[5] | Martin Lepage[4] | Benoit Paquette[1] | Maxime Descoteaux[4,7]**

[1] Center for Research in Radiotherapy, Department of Nuclear Medicine and Radiobiology, Université de Sherbrooke, Sherbrooke, Québec, Canada

[2] Service of Radiation Oncology, Centre Hospitalier Université de Sherbrooke, Sherbrooke, Québec, Canada

[3] Plateforme d'analyse et visualisation d'images (PAVI), Centre de Recherche du Centre Hospitalier Universitaire de Sherbrooke, Sherbrooke, Québec, Canada

[4] Sherbrooke Molecular Imaging Center, Department of Nuclear Medicine and Radiobiology, Université de Sherbrooke, Sherbrooke, Québec, Canada

[5] Department of Pharmacology and Physiology, Université de Sherbrooke, Sherbrooke, Québec, Canada

[6] Department of Pathology, Centre Hospitalier Universitaire de Sherbrooke, Sherbrooke, Québec, Canada

[7] Department of Computer Science, Université de Sherbrooke, Sherbrooke, Québec, Canada

**Correspondence**
Benoit Paquette, Department of Nuclear Medicine and Radiobiology, Faculty of Medicine and Health Sciences, Université de Sherbrooke, Sherbrooke, Québec, Canada.
Email: Benoit.Paquette@USherbrooke.ca

**Present address**
Julie Constanzo, Strasbourg University, CNRS, IPHC UMR 7178, F-67000, Strasbourg, France

**Funding information**
Fonds de Recherche Québécois – Nature et Technologies, Grant Number: 172009

**Purpose:** The analysis of biological and mesoscopic structures properties by diffusion MRI (dMRI) in brain after radiation therapy remains challenging. In our study, we described the consequences associated with an unwanted dose to healthy tissue, assessing radiation-induced brain alterations of living rats with dMRI compared to histopathology and behavioral assays.

**Methods:** The right primary motor cortex $M_1$ of the rat brain was targeted by stereotactic radiosurgery with a mean radiation dose of 41 Gy. Multidirectional single b-value dMRI data of the whole brain were acquired with a 7T small-animal scanner before irradiation until 110 days post-irradiation. Diffusion tensor imaging metrics, such as fractional anisotropy (FA), mean diffusivity (MD), axial (AD), and radial diffusivity (RD) were compared to brain alterations detected by immunohistochemistry and motor performances measured by a behavioral test.

**Results:** Between days 90 and 110, radiation necrosis was observed into the white matter spreading into $M_1$. Results showed a reduction of FA in the corpus callosum and in the striatum, which was driven by an increase in RD from 90 to 110 days post-irradiation, whereas only RD increased in $M_1$. Values of RD and AD increased in the irradiated hippocampus, while FA remained constant. Moreover, an increased MD, AD and RD was observed in the hippocampus that was probably related to inflammation as well as reactive astrogliosis after 110 days post-irradiation. Finally, rats did not exhibit locomotor deficits.

**Conclusions:** dMRI metrics can assess brain damage; the sensitivity of dMRI metrics depends on the brain region.

**KEYWORDS**
diffusion MRI, diffusion tensor imaging (DTI), Gamma Knife, radiation necrosis, small-animal

  

## 1 | INTRODUCTION

Radiotherapy is frequently used to treat primary brain tumor or metastasis. Unfortunately, treatment planning must be improved because <5% of glioblastoma patients survive more than 5 years,[1] whereas the median survival time is ∼5–25 months in patients with brain metastasis.[2,3] Limited knowledge is available on the probability to induce brain damage and behavioral alterations depending on the radiation dose, the tumor location, and the volume to irradiate, and therefore such considerations are not included in treatment planning. Stereotactic radiosurgery (SRS) consists in delivering a high single or hypofractionated dose on small brain tumor or metastasis. Although accuracy of the dose deposition is high, clinical complications are often reported, such as delayed formation of edema in the irradiated volume,[4] and in some cases, development of necrosis.[4,5]

Diffusion magnetic resonance imaging (dMRI) is a non-invasive technique uniquely capable of quantifying the diffusion process of water molecules in *living* biological tissues.[6] The extent and direction of water diffusion within brain structures depend on tissue microstructure and organization. Therefore, diffusion tensor imaging (DTI),[7] is widely used to map brain architecture, usually characterizing the effects of disease and aging principally on the white matter, for example.[8,9] It is also possible to determine for each voxel of the image the fractional anisotropy (FA)[10–12] and the mean diffusivity (MD) representing mean molecular motion that is incoherent at the scale of an imaging voxel.

Adverse radiation effects in the brain have triggered clinical and preclinical studies to better define with dMRI the outcomes of different irradiation paradigms on mesoscopic structure properties. For example, local white matter damage was observed in patients by DTI following radiotherapy for nasopharyngeal carcinoma.[13] The authors found a lower FA and a higher MD in the normal-appearing white matter within 6 months after radiotherapy, which they tentatively explained as reflecting transient cerebral edema and demyelination. In addition, a decrease in FA was observed in irradiated rat brain hemisphere in the white matter.[14] However, these authors reported an increase or a decrease in radial and axial diffusivity associated to histological evidence of demyelination, reactive astrogliosis and necrosis of the white matter, as observed over an extensive range of post-irradiation delays. This was in contradiction with an earlier report of Harsan et al.[9] where an increase in radial and axial diffusivity was observed after dysmyelination and astrocytes hypertrophy in a mouse model of central nervous system disorder. Recently, in a mouse model, perilesional edema was observed by DTI after a single radiation dose of 50 Gy (50% isodose) in an hemisphere.[15] A hyperintense signal observed on MD maps at 12 weeks in the contralateral hemisphere (dose < 25 Gy) was ascribed to damaged fibers originating from the irradiated hemisphere and connecting into the contralateral hemisphere. Clearly, a coherent interpretation of the variation of DTI metrics in white matter is not available. Moreover, only sparse reports focused on radiation-induced grey matter damage, as for example Horská et al.,[16] who studied subcortical changes (including the hippocampus and the striatum) after cranial radiation therapy in children.

We previously validated the usefulness of $T_2^*$-weighted images for the detection of radiation necrosis and measured blood vessel permeability using dynamic contrast-enhanced MRI in the same animal model.[4] The onset of radiation necrosis being dose-dependent, as demonstrated by Jiang et al.,[17] our animal model received a high dose of radiation that enabled us to observe damage after a short delay. The purpose of this study is to describe the consequences associated with an unwanted dose to healthy tissue, using quantitative analysis of radiation-induced mesoscopic alterations in the brain, including white matter and the grey matter structures, of living rats with dMRI. Several DTI measures were compared to histopathology and behavioral assays focused on white and grey matter, including $M_1$-specific response to radiation.

## 2 | METHODS

### 2.1 | Irradiation of Fischer rat brain

The experimental protocol was approved by the Institutional Ethical Committee of the Université de Sherbrooke and complied with regulations of the Canadian Council on Animal Care (protocol #363-14). Twenty-five male Fischer rats (∼250 g) were anesthetized with propofol (10 mg/mL; rate: 1700 μL/h). Eight sham-irradiated rats served as behavioral controls. Seventeen rats (5 rats for imaging and 12 rats for behavioral tests) were irradiated, targeting the primary motor cortex ($M_1$) of the right hemisphere with a Leksell Gamma Knife Perfexion (Elekta AB, Stockholm, Sweden), as previously described.[18] This area was targeted in accordance with the observation that human brain tumors are frequently located in the frontal and parietal lobes,[19] whose border between these 2 areas includes primary somatosensory and motor cortices. A single isocenter treatment plan delivered 37 Gy at the 30% isodose line of the target volume (6 $mm^3$) with 4-mm diameter collimators (Figure 1). The rat brain is more radio-resistant compared to human explaining this high dose of radiation, as previously described by Kondziolka et al.[20] Based on dose–volume histograms calculated by GammaPlan (Elekta AB, Stockholm, Sweden), the mean doses delivered were: $41 \pm 8$ Gy in $M_1$, $35 \pm 5$ Gy in the striatum, and $24 \pm 10$ Gy in the hippocampus volume.[18] On days 110 or 140 post-irradiation, animals were deeply anesthetized with ketamine/xylazine (87:13 mg/mL) and then

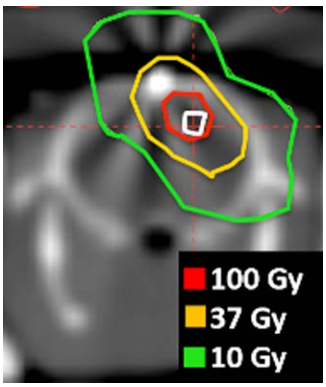


**FIGURE 1** Prescribed treatment plan simulated by GammaPlan© in an axial plan. The yellow isodose is the 37 Gy prescription dose

euthanized via intracardiac perfusion with 4% paraformaldehyde. Rat brains were cryoprotected in a serial gradient of buffered sucrose (30%) and sectioned axially (30 µm thick) using a microtome (SM2000R, Leica, Wetzlar, Germany) or protected in ethanol before being paraffin-embedded and axially sectioned (4 µm).

## 2.2 | In vivo MRI

Five rats were anesthetized with 5% isoflurane in oxygen and maintained at 2–2.5% isoflurane in oxygen (1.5 L/min). Then, rats were scanned using a 7T small animal scanner (Varian, Palo Alto, CA) with a dedicated rat head surface coil (2 elements) (RAPID MR International, Columbus, OH) before irradiation ($N = 4$ because of a technical limitation), on days 10 ($N = 5$), 54 ($N = 5$), 90 ($N = 5$), and 110 ($N = 4$, because of a technical limitation). The air temperature around the animals was maintained constant at 30 °C with a warm-air heating system (SA Instruments, Stony Brook, NY). In addition, for each MR sequence, the first or second slice was placed at the interface of the olfactory bulb and the brain, which was visible in the sagittal view of scout images.

DWI were acquired using a multi-slice spin echo sequence with 15 non-collinear uniform diffusion gradient directions and b = 977 s/mm$^2$. A reference b = 0 image was also acquired. Other imaging parameters were: $\Delta = 14$ ms, $\delta = 6.3$ ms, gradient amplitude 17 T/m, TR/TE = 3500 ms/35 ms, FOV = $38.4 \times 38.4$ mm$^2$, 25 contiguous coronal slices, $0.3 \times 0.3 \times 0.35$ mm$^3$ resolution, for a 2 h total scan duration. An EPI sequence would have reduced the acquisition time at the expense of geometric distortions.

A fast spin echo $T_2$-weighted ($T_2$-w) sequence was performed with the following parameters: TR = 3000 ms; effective echo time $TE_{eff} = 48$ ms; 8 echoes; echo spacing 12 ms; FOV = $32 \times 32$ mm$^2$, 25 slices, 0.7 mm axial slice thickness.

The $T_2^*$ w imaging sequence was a 3D gradient echo sequence, which was performed with TR = 90 ms; TE = 25 ms; FOV = $3 \times 3 \times 1.5$ mm$^3$; resolution: $0.117 \times 0.117 \times 0.156$ mm$^3$; flip angle: 15 °; 2 averages.

## 2.3 | Diffusion MRI pre-processing steps

Field homogeneity artifacts were corrected on each diffusion-weighted image with a N4 bias field correction to normalize the image intensity.[21] Next, non-local means (NLM) denoising was applied to correct the Rician noise bias.[22] The noise SD was estimated directly from the data, and the denoising was performed separately and sequentially on each diffusion-weighted volume. Inconsistent image intensity was observed for odd and even images linked to the interleaved acquisition of thin slices (350 µm) without gap. In a first approximation, these variations affect the whole image in the same fashion such that a simple correction factor could normalize the intensities. Using the cortical ROI from a rat brain atlas,[23] the mean intensity of the even (M_even) and odd (M_odd) slices were computed. Then, a correction factor *f* was applied to the odd slices, with f = M_odd/M_even. Details, raw data, and corrected data will be made available on request. Finally, motion artifacts were minor or absent in our data sets. Motion-correction was still tested but resulted in over-blurring such that this step was omitted.

## 2.4 | Local diffusion MRI reconstruction of DTI measures

From our isotropic diffusion-weighted data set, in-house DTI reconstruction[24] were performed using the Dipy library.[25] First, a non-negative least square method was used to compute the diffusion tensors and local DTI measures such as FA between 0 and 1 and diffusivities AD, RD, MD (axial, radial, mean diffusivities) in mm$^2 \times$ s$^{-1}$. The non-negative least-square ensured positive definite tensor reconstruction and avoided degenerate tensors with negative eigenvalues and FA values above 1. Figure 2 shows representative DTI reconstructions.

## 2.5 | ROI-based method

The rat brain was divided in 2 main anatomical areas: the cortex and the white matter into the right (irradiated) and the left (non-irradiated) hemispheres. DTI measures were calculated for specific ROIs in each of these structures, including primary motor cortex, the hippocampus, the striatum (caudate putamen), the corpus callosum (CC), and the fimbria of the hippocampus (Figure 3). The ROIs were determined using a rat brain atlas[23] registered to diffusion-weighted images. For each time point, the atlas is linearly registered on the b0 with FLIRT[26] and then non-linearly with ANTS.[27] Then, we apply the transformation sequence found at the ROIs in the atlas space to bring them into the diffusion space. Ventricles became enlarged and contaminated nearby ROIs. To avoid CSF contamination, a thresholding was performed as follows. First, the average CSF signal and associated SD were measured by manually segmenting a small volume of the

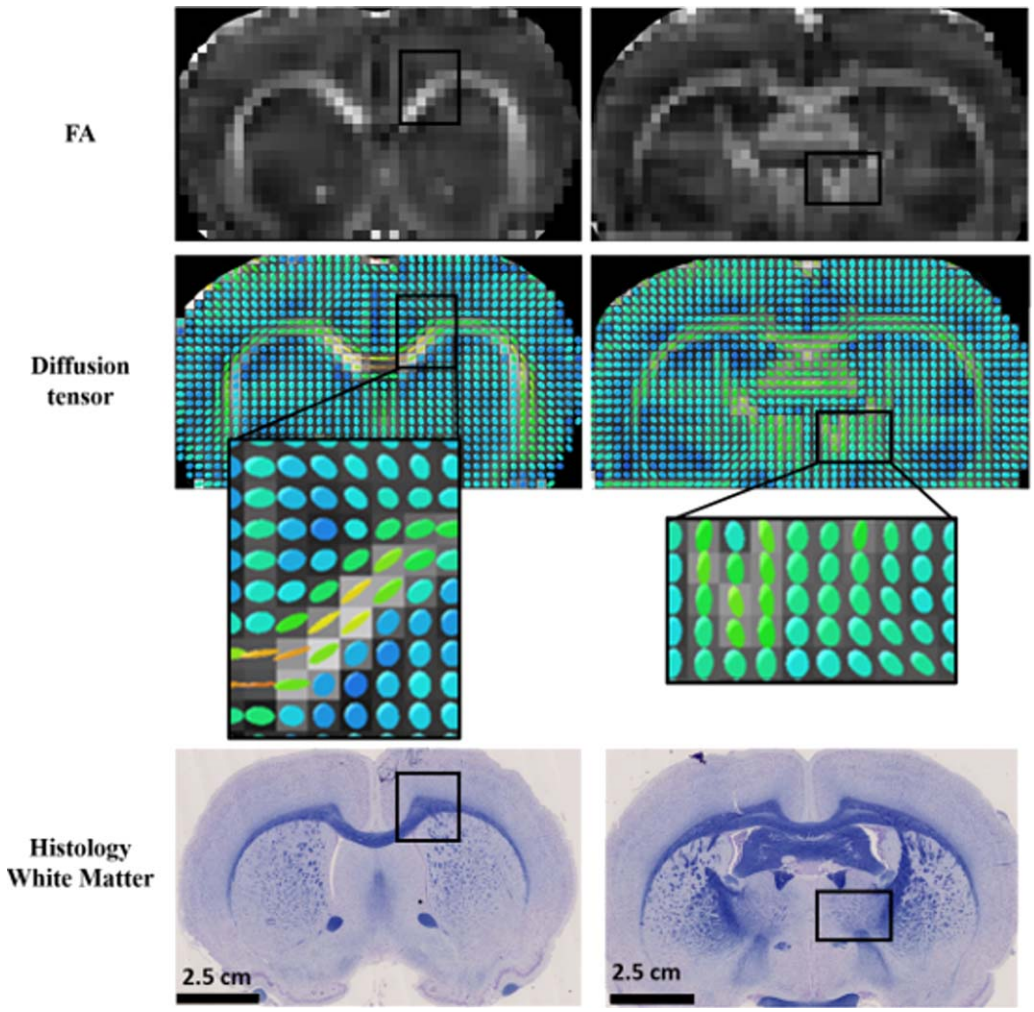


**FIGURE 2** DTI measures compared to histology of the white matter (Luxol fast blue staining). From the diffusion tensors, several tissue measures or maps were extracted such as the fractional anisotropy (FA) and diffusivities (mean, axial and radial). The left column shows a slice located at Bregma = 1.08 mm. The zoom-in area includes a part of the CC and the neocortex. The right column shows a slice located at Bregma = −1.20 mm with a zoom-in area including a part of the subcortex (mainly the thalamus including basal nucleus)

ventricles on each b = 0 data set (each animal, each time point). Then, all voxels with intensity above mean CSF signal minus 1 SD were removed from all subsequent analysis.

## 2.6 | Behavioral tests

$M_1$ was irradiated with a single high dose of radiation using a Gamma Knife. Several brain structures surrounding $M_1$, such as the striatum involved in voluntary motor control and the hippocampus associated to spatial memory, also received radiation and was monitored before irradiation until 110 days post-irradiation.[4] The hippocampus served as a brain structure of reference to assess the level of radiation toxicity in $M_1$ because its high radiation sensitivity was previously established in clinical and preclinical studies.[28–30]

Locomotion was measured by an actimetry test on days 54, 82, and 110 in irradiated and non-irradiated control rats with the MotorMonitor Version 5.05 (Kinder Scientific, Poway, CA). The ambulatory functions were measured by individually placing animals into a clear cage and their movements were scored with infrared beam-mounted sensors racks for 16 h starting at noon. Parameters analyzed were basic movements determined by the occurrence of X and Y beam breaks.

## 2.7 | Histopathology

Control and irradiated rat brains were analyzed on days 110 and 140. The microglial/macrophage (Iba-1) and the astrocyte (GFAP) response to radiation, the brain tissue structure (hematoxylin and eosin [H&E]), and the myelin sheaths (Luxol fast blue) were performed as previously described in Constanzo et al.[4] Finally, sections were examined with a slide scanner (Nanozoomer 2.0-RS, Hamamatsu, Boston, MA) combined with Nanozoomer Digital Pathology software (NDP.view2).

## 2.8 | Statistical analysis

Data were expressed as mean ± SD except for behavioral tests expressed as mean ± standard error of the mean (SEM).

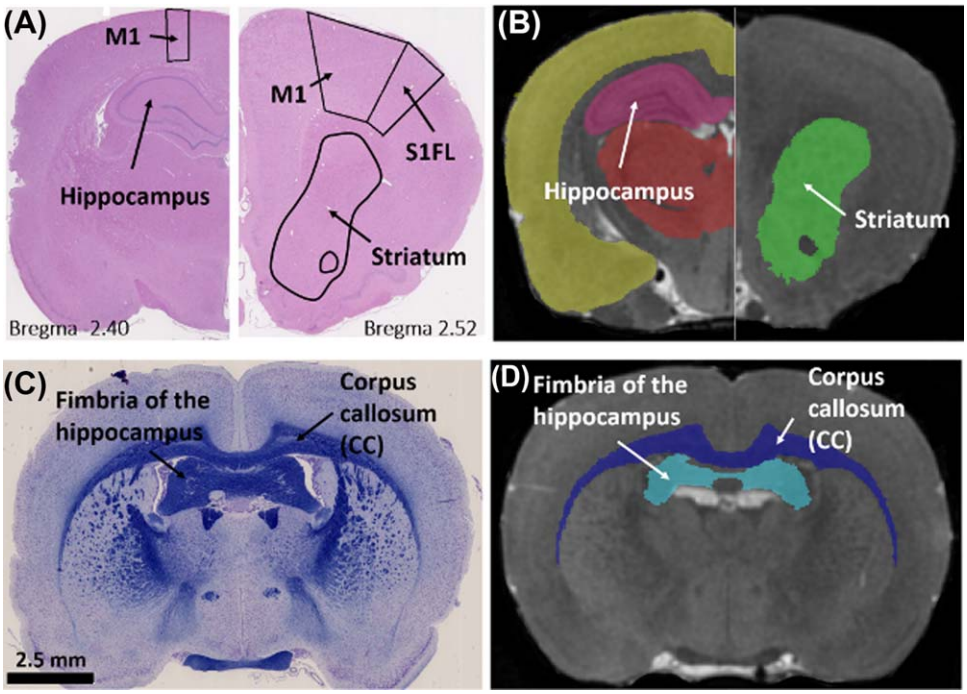


**FIGURE 3** Regions of interest chosen to perform DTI data extraction (ROI-based method). These ROIs are shown on histology slides (A) H&E and (C) Luxol Fast Blue and on $T_2$-w with the rat brain atlas mask (B and D)

Statistics for behavioral experiments comparing irradiated and non-irradiated control groups were performed using non-parametric Mann-Whitney tests. For quantitative dMRI analysis, measurements on irradiated and non-irradiated hemispheres of 5 brain ROI at 5 different time points were performed on every animal. Because the number of animals is small ($N = 5$), analyzes were decomposed into 2 nonparametric tests. First, a Friedman test (two-tailed, paired repeated measures) was done to test the effect of time by region and radiation. For this test, the comparison was performed between days 10 and 110 because 1 rat could not be scanned at baseline. Second, the effect of radiation as a function of time and region was tested with a paired Wilcoxon tests (one-tailed paired test). A $P$-value $\leq 0.05$ was considered to be significant. Calculations were performed with GraphPad Prism 7.0 (GraphPad Software, La Jolla, CA).

## 3 | RESULTS

### 3.1 | White matter changes following irradiation

Figure 4 shows DTI measures in CC and fimbria as a function of time. Our first observation is that the control CC and fimbria had very stable values of FA, MD, RD, and AD from days 0 to 54, which provides confidence that the scanner performance was constant. Between days 10 to 110, the FA decreased for both structures (***$P = 0.0002$), the MD increased (*$P = 0.03$, Fimbria; *$P = 0.04$, CC), as well as the RD (***$P = 0.0006$, Fimbria; **$P = 0.0014$, CC) and the AD for the corpus callosum (*$P = 0.016$, CC) (Figure 4).

The effect of radiation into the CC, was mainly because of the necrosis that led to, e.g., a decrease of the tissue anisotropy of −25% on day 110 (*$P = 0.03$), therefore no inflammation was observed (no changes in MD) between contralateral and irradiated CC (Figure 4). However, the RD increased in the irradiated CC on day 90 (*$P = 0.03$), reaching 11% on day 110 (*$P = 0.03$) compared to its contralateral counterpart, while the AD decreased on day 90 (*$P = 0.03$) (day 110, $P = 0.06$). The scenario into the fimbria was quite different. The inflammation (MD-related) was significantly increased in the irradiated fimbria on day 90 (*$P = 0.03$). A trend to higher RD was observed on days 90 and 110 but was not significant ($P = 0.06$) (Fig. 4). On day 110, the control fimbria metrics also varied, explaining the non-significant variation in MD and RD for this time point. Although the AD was constant over time, it was affected by the lesion (necrosis spreading) on day 110, leading to 17% less axial orientation of fibers (*$P = 0.03$) (Figure 4).

### 3.2 | Grey matter changes following irradiation

The raw diffusion-weighted images were examined before statistical analysis to avoid misinterpretation of results. As b0 images are essentially $T_2$-weighted, abnormal intensity mainly reflects iron deposits (hypointensity) and edema (hyperintensity) that can occur in and around necrotic area (Figure 5A). After removing hyperintense CSF

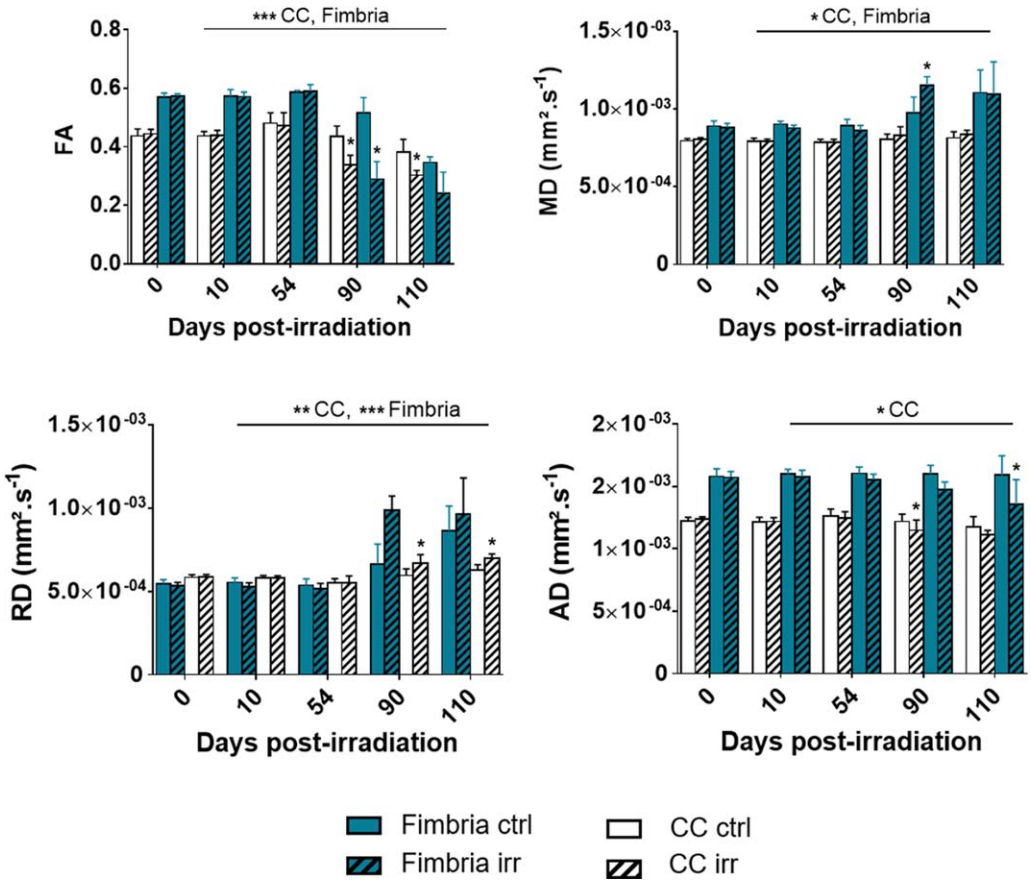


**FIGURE 4** Standard measures calculated from white matter ROIs. *Ctrl* corresponds to the contralateral hemisphere (solid pattern), and *irr* corresponds to the irradiated hemisphere (hatched pattern). dMRI group $N = 5$ (pre- and day 110 post-irradiation, $N = 4$). All data represent mean ± SD. Statistical analyses consisted of a Friedman test, assessing variations over experimental time line compared to the baseline (day 0) (horizontal bars over histograms), and a Wilcoxon test to assess differences between each ROI located in contralateral and irradiated hemispheres (stars over hatched pattern bars)

contamination into the atlas-derived ROIs, perilesional hyperintensity on MD maps observed on days 90 (data not shown) and 110 post-irradiation (Figure 5B) was ascribed to edema (inflammation), qualitatively corresponding on day 140 to the activation of microglia/macrophage in response to inflammation (brown Iba-1 staining) (Figure 5C).

The values of FA decreased significantly over time in the irradiated $M_1$ ($^{**}P = 0.0087$); however, no significant difference was observed with the contralateral $M_1$ when the severity of the lesion increased on days 90 and 110 (Figure 6). This result may be explained by the relatively low dose of radiation received by this structure ($D_{M1\text{-contralateral}} = 21 \pm 3$ Gy) that would lead to a decrease of FA in the contralateral structure. Conversely, the values of MD remained constant in irradiated $M_1$ over the experimental time course and compared to its contralateral counterpart. However, the radial orientation of fibers in $M_1$ was significantly affected by the lesion from days 10 to 110 ($^{***}P = 0.0006$). RD increased on day 90 ($^{*}P = 0.03$) up to 46% on day 110 ($^{*}P = 0.03$) in irradiated $M_1$ compared to the contralateral, whereas a slight increase was observed in AD on day 90 ($^{*}P = 0.034$) (day 110, $P = 0.06$) (Figure 6).

In the irradiated hippocampus, FA remained constant over the time whereas a significant increase in MD was observed ($^{***}P = 0.0006$). This was ascribed to the comparable increase of RD and AD over time ($^{*}P = 0.044$ and $^{***}P = 0.0006$, respectively), as well as compared to its contralateral counterpart, respectively 30% and 28% on day 110 ($^{*}P = 0.03$), leading to a 29% increase in MD ($^{*}P = 0.03$) with an unchanged FA in the irradiated hippocampus (Figure 6).

FA in the irradiated striatum decreased significantly over time ($^{**}P = 0.0055$) (Figure 6), which may be associated to a significant increase in RD in the irradiated striatum ($^{**}P = 0.0021$) (Figure 6). In addition, compared to its contralateral structure, FA decreased on day 90 by up to 35% on day 110 ($^{*}P = 0.03$) in the irradiated striatum, while a slight increase was observed in AD on day 90 ($^{*}p = 0.034$) but not significant on day 110, and the RD increased up to 14% on day 110 (Figure 6).

## 3.3 | Specific sensitivity of locomotion-related brain structures to radiation

Daily follow-up of rats did not reveal any locomotor deficit, ataxia, or paralysis. To assess more accurately the locomotion of irradiated rats, their basic movements were recorded with the actimetry test during 16 h on days 54, 82, and 110

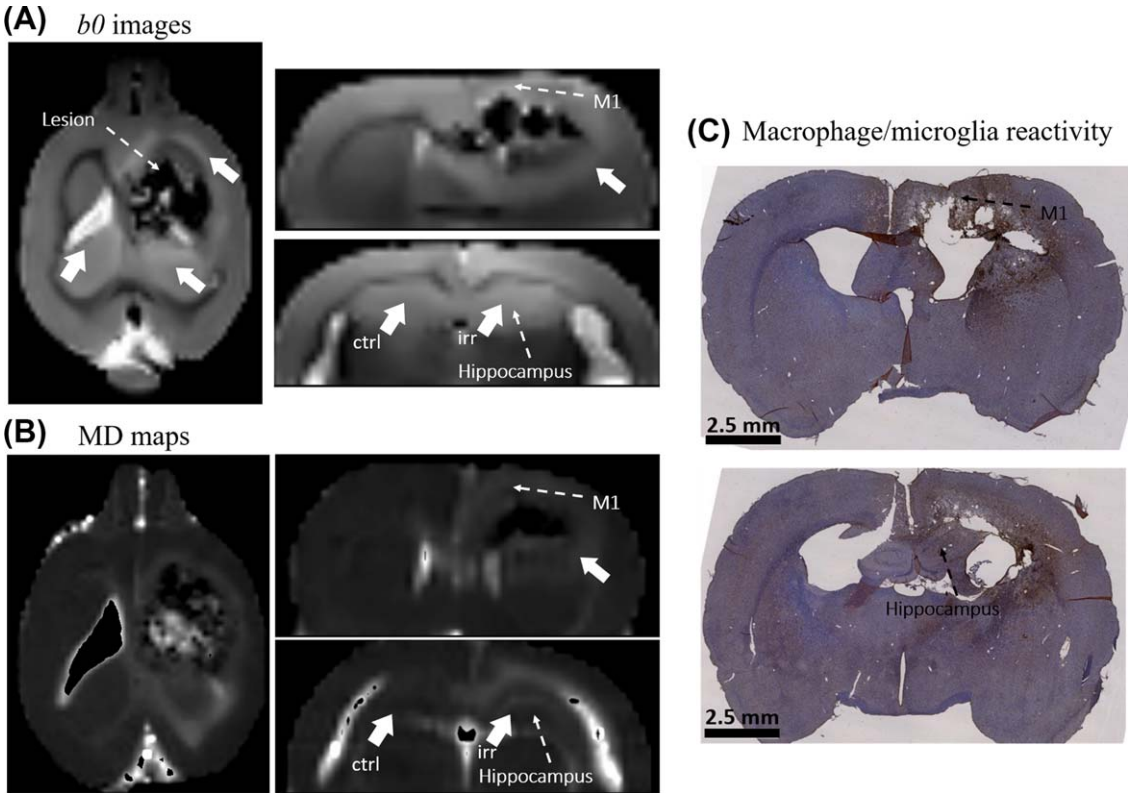


**FIGURE 5** Evidence of inflammation and necrosis. (A) b0 raw images and (B) MD maps on day 110 post-irradiation compared to (C) Iba-1 staining (brown) indicates the up-regulation of microglia and macrophages on day 140 (counterstained with hematoxylin)

after irradiation (Figure 7). This test did not discriminate the contribution of the striatum (involved in voluntary motor control) from $M_1$ in the locomotor performance, but provided evidence that irradiated rats had no dysfunction concerning basic movements. On the contrary, the measure of locomotor activity reveals the presence of a hyperactive state on days 82 and 110 (****$P < 0.0001$) (Figure 7).

Tissue-specific sensitivity was observed with histology. First, necrosis was observed mainly in the corpus callosum (H&E and Luxol fast blue staining) (Figure 8A) (compare damage to before irradiation in Figure 1), into $M_1$ (Figures 8A and 8B), and surrounding the hippocampus (Figure 8C) using H&E staining. In addition, demyelination was observed in the white matter specifically in the external capsule (Figure 8A). GFAP staining further revealed reactive astrogliosis in irradiated regions, as observed in $M_1$ and in the hippocampus (see zoom-in boxes 1, 2, 4, and 5 in Figures 8B and 8C). In the $M_1$ area, which received a mean dose of 41 Gy, different gradation of reactive astrogliosis can be observed: moderately reactive astrogliosis (astrocytes diameter $\approx$ 50 μm), in which most astrocytes have up-regulated expression of GFAP and exhibit cellular hypertrophy, and severe diffuse reactive astrogliosis (astrocytes diameter $\approx$ 100 μm) with pronounced up-regulation of GFAP expression, astrocyte hypertrophy, astrocyte proliferation, and pronounced overlap of astrocyte processes. No severe reactivity was observed in the hippocampus, but only moderate reactive astrogliosis (astrocytes diameter $\approx$ 80 μm) (compare zoom-in boxes 4 and 5 of Figure 8C).

## 4 | DISCUSSION

We have determined the capacity of dMRI to detect modifications in specific brain structures in a living rat model that mimics the late-delayed necrosis observed after irradiation into the white and grey matter. The aim of this study was to extract quantitative information from brain anatomical images (diffusion tensor imaging metrics) and to associate them with their corresponding preclinical endpoints (e.g., radiation necrosis, behavioral changes, inflammation).

The mean doses delivered to the grey matter were: 41 ± 8 Gy in M1, 35 ± 5 Gy in the striatum, and 24 ± 10 Gy in the hippocampus volume. The corpus callosum located under $M_1$ and the fimbria of the hippocampus received a comparable radiation dose. H&E and Luxol fast blue staining demonstrated necrosis mainly located in the white matter, causing axonal disruption (corpus callosum) associated with demyelination (external capsule). It is noteworthy that the FA and AD were higher for the fimbria than for the CC. The fimbria of hippocampus observed on histological staining (Figure 3) shows fibers axially oriented, whereas the CC is characterized by crossing fibers with neurons and the internal capsule

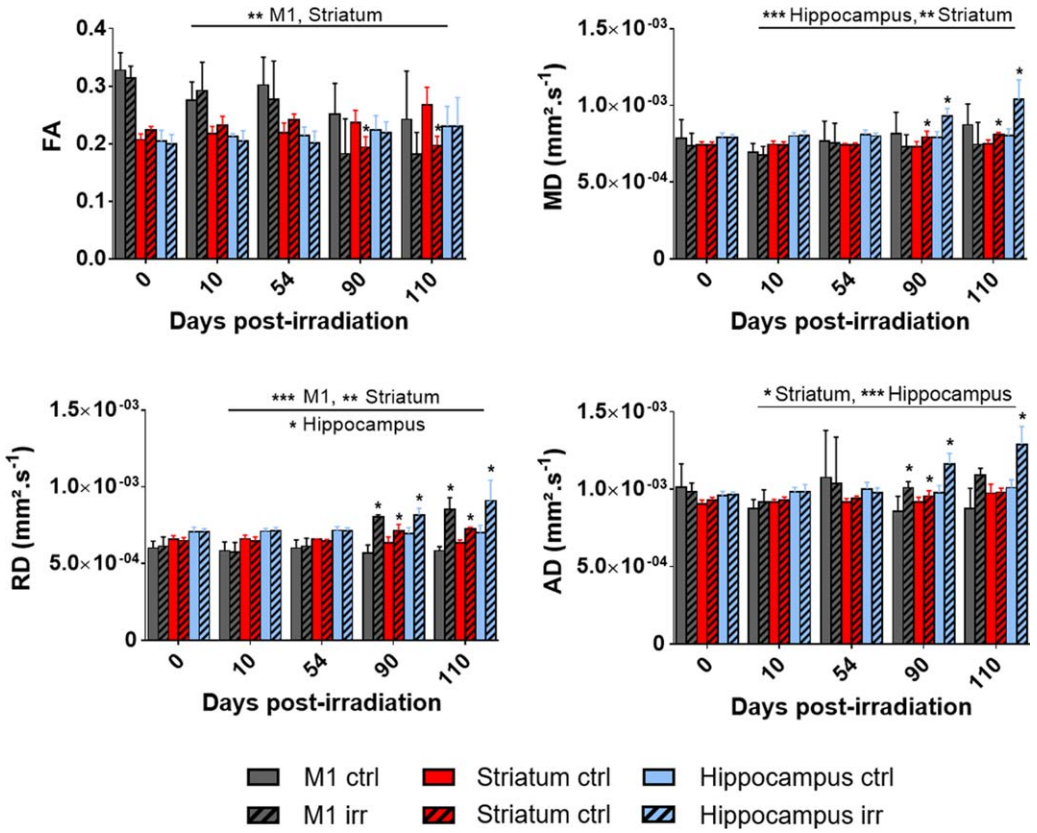


**FIGURE 6** Standard measures calculated from grey matter ROIs. *Ctrl* corresponds to the contralateral hemisphere, and *irr* corresponds to the irradiated hemisphere (filled pattern). dMRI group $N = 5$ (pre- and day 110 post-irradiation, $N = 4$). All data represent mean ± SD. Statistical analyses consisted of a Friedman test, assessing variations over experimental time line compared to the baseline (day 0) (horizontal bars over histograms) and a Wilcoxon test to assess differences between each ROI located in contralateral and irradiated hemispheres (stars over hatched pattern bars)

probably leading to a lower signal in DTI measures because of a complex tensor shape. Histopathology analysis also revealed tissue microstructural changes into $M_1$, the striatum, and the hippocampus with different severity gradation. $M_1$ received the highest radiation dose but it was not the structure the most affected, with changes observed only in RD (compared to the contralateral) on day 110 following irradiation. The irradiated striatum demonstrated 35% decreased FA, 8% increased MD, and 14% increased RD on day 110 compared to the contralateral striatum. Although $M_1$ and striatum are related to locomotion, irradiated rats had no dysfunction concerning basic movements. However, despite a constant FA over the experimental time course, and even though it had received the lowest dose, the hippocampus was the most affected structure with MD increased by 29%, AD increased by 28%, and RD increased by 30% compared to the contralateral hippocampus on day 110. This is consistent with a previous report using the same animal model in the same conditions where rats demonstrated a spatial memory decline.[4] The tissue surrounding the necrotic area was

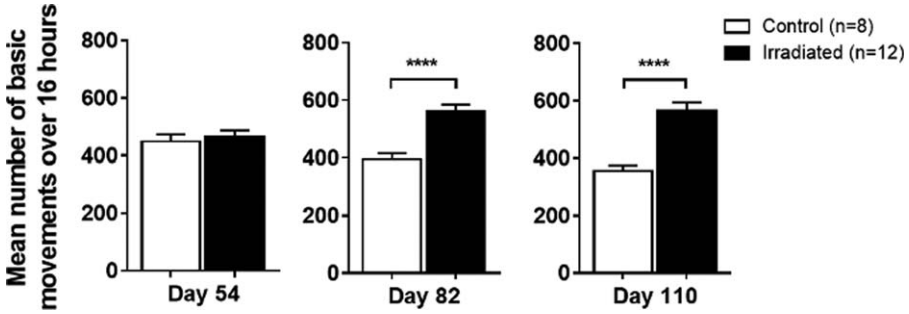


**FIGURE 7** Effects of irradiation of the primary motor cortex ($M_1$) on basic movements. $M_1$ sensitivity to radiation was measured with a behavioral test assessing motor function (Actimetry) 54, 82, and 109 days after radiation exposure. The locomotor basic movements of the rats were recorded during a 16-h period (including the active phase) and revealed hyperactivity on days 82 and 110 (****$P < 0.0001$). Control group (sham-irradiated) $N = 8$, and irradiated group $N = 1$ 2. All data represent mean ± SEM. Statistical analysis consisted of nonparametric Mann-Whitney tests

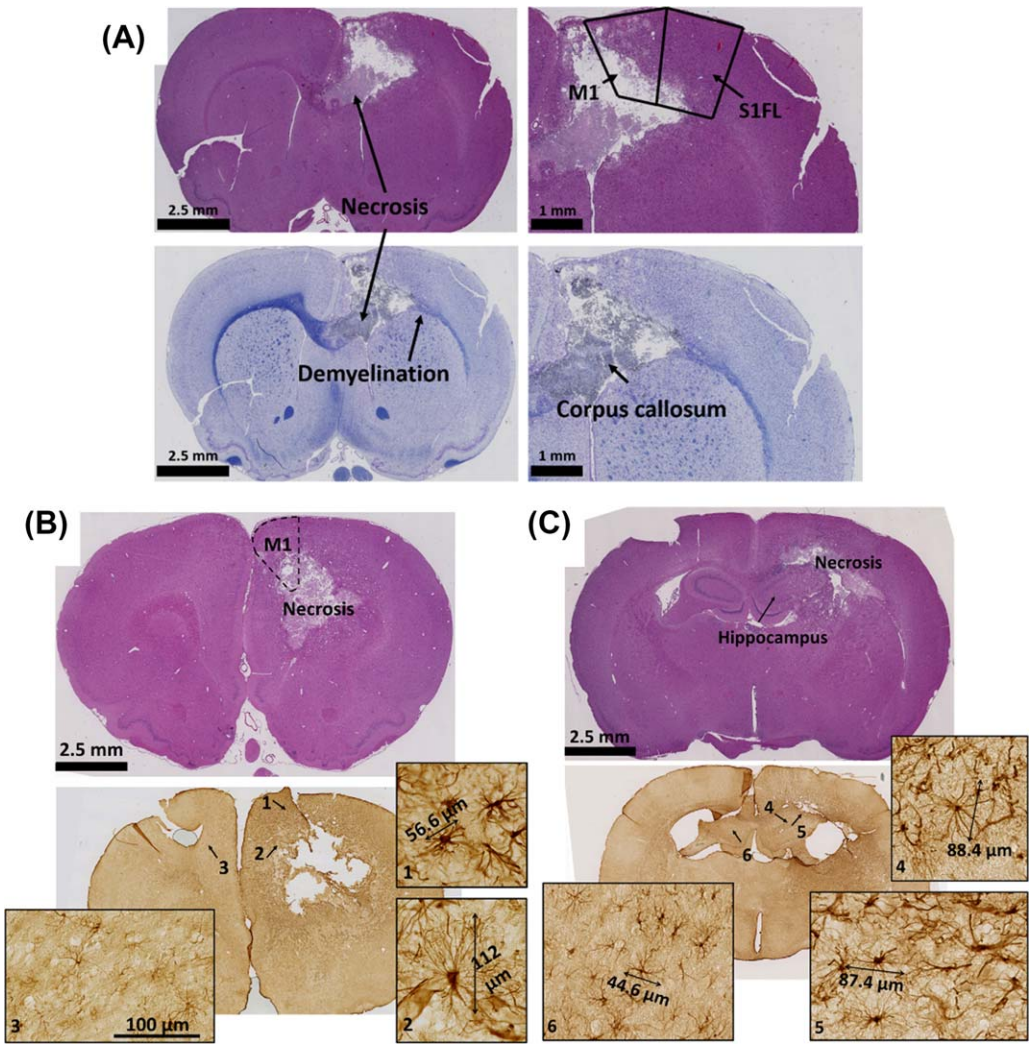


**FIGURE 8** Necrosis and demyelination on day 110 post-irradiation. The H&E staining (top) shows necrosis mainly located in the white matter and the grey matter ($M_1$ and primary somatosensory, S1FL). The Luxol fast blue staining (bottom) highlights axonal disruption in the corpus callosum and demyelination further in the white matter (external capsule).

characterized by the presence of inflammation, which was paralleled by a decreased anisotropy and/or increased MD.

Compared to the contralateral counterparts, our results demonstrated a decreased FA in the irradiated CC mainly because of an increase of the radial diffusivity on day 110, whereas no changes in FA for the fimbria were observed despite a decrease of AD. As observed for CC, values of RD increased in the irradiated striatum (no changes in AD) on day 110 seemed causing the observed decrease in FA. The impact on FA caused by changes of RD and AD was previously reported by Wang et al.,[14] who monitored with DTI the radiation-induced white matter damage (in the external capsule) after a 30 Gy irradiation in a brain hemisphere of rats. They reported that the reduction in FA was mainly driven by a decrease in AD in the earlier phase (4–16 weeks post-irradiation) and by an increase in RD and return to baseline in AD in the late phase (48 weeks post-irradiation). Interpretation of their results is not straightforward, as it appears that the radial and the axial diffusivities *decreased* to a larger extent in the contralateral hemisphere compared to the irradiated hemisphere out to 48 weeks. This may suggest that these metrics normally decrease with age but they decrease to a lesser extent after a radiation dose; the net impact of the dose would then be to *increase* the diffusivities. This interpretation is supported by Löbel et al.,[31] who observed diffusion declined in all 3 directions with age mainly in the corpus callosum and the internal capsule, leading to a decrease of RD and AD. Our study monitored animals for a much shorter period of 16 weeks (because the higher radiation dose shortened the delay before damage is detectable) and the effects of aging were therefore comparatively unimportant. Our results suggest that radiation-induced alteration of FA in both grey and white matter is strongly influenced by changes in radial diffusivity. However, values of RD and AD *increased* in the irradiated hippocampus on days 90 and 110, whereas FA remained constant. Consequently, changes in radial and axial tensors shape varied concertedly such that FA remained constant.

Our choice of using objective ROIs has the advantage that the procedure is reproducible and unbiased; it may be transferable to clinical application, as performed by Horská et al.[16] and Kassubek et al.,[32] who kept the same registered ROIs throughout the longitudinal assessment of patients, and it can be reproduced by other research groups. Moreover, the CSF signal intensity in every image were excluded from ROIs to avoid misinterpretation of results because of lesion-induced ventricles swelling and disruption (Figure 5).

Moderate reactive astrogliosis is generally associated with mild nonpenetrating trauma in areas distant to focal brain lesions.[33] In severe diffuse reactive astrogliosis, there is pronounced up-regulation of GFAP expression, with pronounced hypertrophy of cell body and processes, as well as astrocyte proliferation, resulting in agglutinating and overlapping of neighboring astrocyte processes (Figure 8).[33] In our study, reactive astrogliosis can be because of necrosis but also because of the permeable neovascularization that we observed in the same animal model using $T_2^*$ w coupled to DCE-MRI.[4] Astrogliosis was also assessed by Wang et al.[14] It did not progress significantly with time after irradiation (for both 25 and 30 Gy) as judged from their GFAP staining results. Moreover, the Luxol fast blue staining, usually used to highlight radiation-induced necrosis and demyelination, decreased only at late time point (48 weeks) for the 30 Gy radiation dose.[14] This result is difficult to interpret as we cannot dissociate radiation necrosis from age-related demyelination. In contrast, Harsan et al.[9] correlated the increase of both RD and AD with the increase of astrocyte hypertrophy located in the white matter (7 affected mice and 7 controls). Our study did not include quantitative histology, however, it is clear that radiation necrosis is surrounded by astrocytes and microglia most likely because of extensive inflammation associated to the severity of the lesion (Figures 5 and 7). In a recent article, Perez-Torres et al.[15] reported on radiation-induced necrosis following a 50 Gy focal irradiation in an hemisphere. After 12 weeks post-irradiation, they observed edema on $T_2$-w images as well as hyperintense signal on MD maps into the neocortex and the hippocampus. Our study confirms the results of Harsan et al.[9] and of Perez-Torres et al.[15] We have previously observed hypointense signals attributed to iron deposits on $T_2^*$ w images.[4] Although it can be easily rationalized that edema can cause an increase of MD without necessarily affecting mesoscopic changes, the effect on DTI measures of strong dephasing caused by iron deposits remain unclear. A detailed understanding of this effect is beyond the scope of the present report.

In this study, elevated MD was observed in the irradiated hippocampus (24 Gy) region on days 90 and 110, and a decreased learning spatial memory (longer escape latency in the Morris water maze task) was observed on day 134 on the same animal model as previously published.[4] This could suggest that an elevated MD corresponds to changes in the brain functional response to radiation. We did not see changes in MD related to a severe and extended lesion in the irradiated $M_1$, and behavioral tests provided evidence that irradiated rats had no mean basic movements dysfunction (actimetry test), although MD increased (3.5 times less than in the hippocampus) in the striatum (related to locomotion). First, this result suggests that there is no radiation-induced brain plasticity in this region, as defined by a transitory state of motricity decline followed by a recovery, but more likely a probable reserve capacity of neurons in $M_1$. Second, this result demonstrates that MD alone cannot fully highlight a relationship between mesoscopic and neurofunctional changes, as also demonstrated by Horská et al.[16] in children who received cranial radiation therapy. Indeed, they studied radiation-induced changes in subcortical mesostructures and showed that elevated MD in the hippocampus was not accompanied by impairment on the visual–spatial working memory performance (bead memory test), whereas performance on the gross motor dexterity and coordination (Purdue pegboard test) declined with increasing MD in the globus pallidus and striatum, suggesting a relationship between motor function and mesostructure of regions of the basal ganglia. Overall, our results suggest that radiation induces region-specific changes in the behavioral response, associated to differences in tissue sensitivity.

## 5 | CONCLUSION

In this study, we compared radiation-induced mesoscopic changes in the rat brain measured by DTI measures with histopathology and behavioral tests. Between days 90 and 110 following irradiation, necrosis and hemorrhage were observed into the corpus callosum (decrease of FA) and into the primary motor cortex ($M_1$) of the hemisphere that received a high radiation dose, where only the radial diffusivity was affected. Inflammation, most likely associated to reactive astrogliosis, and an increase of MD, AD, and RD, were observed in the hippocampus that received lower doses than $M_1$. Our study clearly confirmed the high sensitivity of the hippocampus to radiation, which suggests that hippocampal-sparing radiotherapy planning is of importance to limit radiation exposure of this region. Surprisingly, the motor coordination of the rat was not affected despite the severity and the extent of the lesion located in $M_1$ and the decreased of FA in the striatum. In the future, biophysical modeling,[34,35] multimodal MRI acquisition, as well as multiple b-value dMRI associated with advanced microstructure reconstruction will be critical to get a better picture of the post-irradiation mesoscopic structure modifications and will provide invaluable insight to guide the development of innovative clinical irradiation protocols (e.g., adaptive radiation therapy) for brain tumor patients.

## ACKNOWLEDGMENTS

The authors gratefully acknowledge Karyn Kirby for behavioral tests procedures, Laurent Hubert for the computational and data storage architecture, Dr. Garant from the Biostatistics service for her advice on statistical analysis, and the Electron Microscopy & Histology Research Core of the FMSS at the Université de Sherbrooke for their histology services. Martin Lepage, Laurence Masson-Côté, Benoit Paquette, Philippe Sarret, and Kevin Whittingstall are members of the FRQS-funded Centre de recherche CHUS. This work was supported by the Fonds de Recherche Québécois Nature et Technologies (172009).

## REFERENCES

[1] Ostrom QT, Gittleman H, Fulop J, et al. CBTRUS statistical report: primary brain and central nervous system tumors diagnosed in the United States in 2008-2012. *Neuro Oncol.* 2015;17: iv1-iv62.

[2] Agboola O, Benoit B, Cross P, et al. Prognostic factors derived from recursive partition analysis (RPA) of Radiation Therapy Oncology Group (RTOG) brain metastases trials applied to surgically resected and irradiated brain metastatic cases. *Int J Radiat Oncol Biol Phys.* 1998;42:155-159.

[3] Nieder C, Mehta MP. Prognostic indices for brain metastases – usefulness and challenges. *Radiat Oncol.* 2009;4:10.

[4] Constanzo J, Masson-Côté L, Tremblay L, et al. Understanding the continuum of radionecrosis and vascular disorders in the brain following gamma knife irradiation: an MRI study. *Magn Reson Med.* 2017;78:1420-1431.

[5] Boothe D, Young R, Yamada Y, Prager A, Chan T, Beal K. Bevacizumab as a treatment for radiation necrosis of brain metastases post stereotactic radiosurgery. *Neuro Oncol.* 2013;15: 1257-1263.

[6] Le Bihan D. The "wet mind": water and functional neuroimaging. *Phys Med Biol.* 2007;52:R57-90.

[7] Descoteaux M, Poupon C. *Diffusion-weighted MRI.* In: Belvic D, Belvic K, editors. Comprehensive biomedical physics. Oxford: Elsevier; 2014. p 81-97.

[8] Budde MD, Frank JA. Examining brain microstructure using structure tensor analysis of histological sections. *Neuroimage.* 2012;63:1-10.

[9] Harsan LA, Poulet P, Guignard B, Parizel N, Skoff RP, Ghandour MS. Astrocytic hypertrophy in dysmyelination influences the diffusion anisotropy of white matter. *J Neurosci Res.* 2007;85:935-944.

[10] Basser PJ, Pierpaoli C. Microstructural and physiological features of tissues elucidated by quantitative-diffusion-tensor MRI. *J Magn Reson.* 2011;213:560-570.

[11] Pierpaoli C, Jezzard P, Basser PJ, Barnett A, Di Chiro G. Diffusion tensor MR imaging of the human brain. *Radiology.* 1996; 201:637-648.

[12] Pierpaoli C, Basser PJ. Toward a quantitative assessment of diffusion anisotropy. *Magn Reson Med* 1996;36:893-906.

[13] Duan F, Cheng J, Jiang J, Chang J, Zhang Y, Qiu S. Whole-brain changes in white matter microstructure after radiotherapy for nasopharyngeal carcinoma: a diffusion tensor imaging study. *Eur Arch Otorhinolaryngol.* 2016;273:4453-4459.

[14] Wang S, Wu EX, Qiu D, Leung LHT, Lau HF, Khong PL. Longitudinal diffusion tensor magnetic resonance imaging study of radiation-induced white matter damage in a rat model. *Cancer Res.* 2009;69:1190-1198.

[15] Perez-Torres CJ, Yuan L, Schmidt RE, Rich KM, Ackerman JJH, Garbow JR. Perilesional edema in radiation necrosis reflects axonal degeneration. *Radiat Oncol.* 2015;10:33.

[16] Horská A, Nidecker A, Intrapiromkul J, et al. Diffusion tensor imaging of deep gray matter in children treated for brain malignancies. *Childs Nerv Syst.* 2014;30:631-638.

[17] Jiang X, Yuan L, Engelbach JA, et al. A Gamma-knife-enabled mouse model of cerebral single-hemisphere delayed radiation necrosis. *PLoS One.* 2015;10:e0139596.

[18] Constanzo J, Paquette B, Charest G, Masson-Côté L, Guillot M. Gamma knife irradiation method based on dosimetric controls to target small areas in rat brains. *Med Phys.* 2015;42:2311-2316.

[19] McKinney PA. Brain tumours: incidence, survival, and aetiology. *J Neurol Neurosurg Psychiatry.* 2004;75(Suppl2): ii12-17.

[20] Kondziolka D, Lunsford LD, Claassen D, Maitz AH, Flickinger JC. Radiobiology of radiosurgery: part I. The normal rat brain model. *Neurosurgery.* 1992;31:271-279.

[21] Tustison NJ, Avants BB, Cook PA, et al. N4ITK: improved N3 bias correction. *IEEE Trans Med Imaging.* 2010;29:1310-1320.

[22] Descoteaux M, Wiest-Daesslé N, Prima S, Barillot C, Deriche R. Impact of Rician adapted non-local means filtering on HARDI. *Med Image Comput Comput Assist Interv.* 2008;11: 122-130.

[23] Papp EA, Leergaard TB, Calabrese E, Johnson AG, Bjaalie JG. Waxholm Space atlas of the Sprague Dawley rat brain. *Neuroimage.* 2014;97:374-386.

[24] Descoteaux M, Deriche R, Knosche TR, Anwander A. Deterministic and probabilistic tractography based on complex fibre orientation distributions. *IEEE Trans Med Imaging.* 2009;28: 269-286.

[25] Garyfallidis E, Brett M, Amirbekian B, et al. Dipy, a library for the analysis of diffusion MRI data. *Front Neuroinform.* 2014;8:8.

[26] Jenkinson M, Smith S. A global optimisation method for robust affine registration of brain images. *Med Image Anal.* 2001;5: 143-156.

[27] Avants BB, Tustison N, Song G. Advanced normalization tools (ANTS). *Insight J.* 2009;2:1-35.

[28] Chang EL, Wefel JS, Hess KR, et al. Neurocognition in patients with brain metastases treated with radiosurgery or radiosurgery plus whole-brain irradiation: a randomised controlled trial. *Lancet Oncol.* 2009;10:1037-1044.

[29] Gondi V, Hermann BP, Mehta MP, Tomé WA. Hippocampal dosimetry predicts neurocognitive function impairment after fractionated stereotactic radiotherapy for benign or low-grade adult brain tumors. *Int J Radiat Oncol Biol Phys.* 2012;83: e487-e493.

[30] Monje ML, Toda H, Palmer TD. Inflammatory blockade restores adult hippocampal neurogenesis. *Science.* 2003;302:1760-1765.

[31] Löbel U, Sedlacik J, Güllmar D, Kaiser WA, Reichenbach JR, Mentzel HJ. Diffusion tensor imaging: the normal evolution of ADC, RA, FA, and eigenvalues studied in multiple anatomical regions of the brain. *Neuroradiology.* 2009;51:253-263.

[32] Kassubek R, Gorges M, Westhoff MA, Ludolph AC, Kassubek J, Müller HP. Cerebral microstructural alterations after radiation therapy in high-grade glioma: a diffusion tensor imaging-based study. *Front Neurol.* 2017;8:286.

[33] Sofroniew MV, Vinters HV. Astrocytes: biology and pathology. *Acta Neuropathol.* 2010;119:7-35.

[34] Stanisz GJ, Wright GA, Henkelman RM, Szafer A. An analytical model of restricted diffusion in bovine optic nerve. *Magn Reson Med.* 1997;37:103-111.

[35] Panagiotaki E, Schneider T, Siow B, Hall MG, Lythgoe MF, Alexander DC. Compartment models of the diffusion MR signal in brain white matter: a taxonomy and comparison. *Neuroimage.* 2012;59:2241-2254.

**How to cite this article:** Constanzo J, Dumont M, Lebel R, et al. Diffusion MRI Monitoring of Specific Structures in the Irradiated Rat Brain. *Magn Reson Med.* 2018;00:1–12. https://doi.org/10.1002/mrm.27112